Hyperspectral imagery quality assessment and band reconstruction using the Prophet model.

MA, P., REN, J., GAO, Z., LI, Y. and CHEN, R.

2024

Received: 9 October 2023 | Revised: 16 December 2023 | Accepted: 3 January 2024

CAAI Transactions on Intelligence Technology

DOI: 10.1049/cit2.12373

ORIGINAL RESEARCH

Hyperspectral imagery quality assessment and band reconstruction using the prophet model

Ping Ma[1] | Jinchang Ren[2] | Zhi Gao[3] | Yinhe Li[1] | Rongjun Chen[2]

[1]National Subsea Centre, School of Computing, Engineering and Technology, Robert Gordon University, Aberdeen, UK

[2]School of Computer Science, Guangdong Polytechnic Normal University, Guangzhou, China

[3]School of Remote Sensing and Information Engineering, Wuhan University, Wuhan, China

Correspondence

Jinchang Ren.
Email: j.ren@rgu.ac.uk

Funding information

National Natural Science Foundation Major Project of China, Grant/Award Number: 42192580; Guangdong Province Key Construction Discipline Scientific Research Ability Promotion Project, Grant/Award Number: 2022ZDJS015

Abstract

In Hyperspectral Imaging (HSI), the detrimental influence of noise and distortions on data quality is profound, which has severely affected the following-on analytics and decision-making such as land mapping. This study presents an innovative framework for assessing HSI band quality and reconstructing the low-quality bands, based on the Prophet model. By introducing a comprehensive quality metric to start, the authors approach factors in both spatial and spectral characteristics across local and global scales. This metric effectively captures the intricate noise and distortions inherent in the HSI data. Subsequently, the authors employ the Prophet model to forecast information within the low-quality bands, leveraging insights from neighbouring high-quality bands. To validate the effectiveness of the authors' proposed model, extensive experiments on three publicly available uncorrected datasets are conducted. In a head-to-head comparison, the framework against six state-of-the-art band reconstruction algorithms including three spectral methods, two spatial-spectral methods and one deep learning method is benchmarked. The authors' experiments also delve into strategies for band selection based on quality metrics and the quality evaluation of the reconstructed bands. In addition, the authors assess the classification accuracy utilising these reconstructed bands. In various experiments, the results consistently affirm the efficacy of the authors' method in HSI quality assessment and band reconstruction. Notably, the authors' approach obviates the need for manually prefiltering of noisy bands. This comprehensive framework holds promise in addressing HSI data quality concerns whilst enhancing the overall utility of HSI.

KEYWORDS

hyperspectral, image reconstruction, machine learning

1 | INTRODUCTION

The rapid development of hyperspectral imaging (HSI) technology has garnered significant attention in various fields due to its ability to capture and provide an extensive range of spectral information across the electromagnetic spectrum [1]. This allows for detailed and accurate characterisation and analysis of materials and objects, leading to increasing applications, such as non-destructive measurement [2], data classification [3, 4] and change detection [5].

Due to the limitations of the atmospheric condition, sensor noise, and other environmental factors, certain bands in hyperspectral imaging (HSI) data may exhibit lower quality compared to others, such as the water absorption bands [6, 7]. These bands are susceptible to noise interference, signal distortion, and reduced sensitivity, compromising the accuracy and reliability of subsequent image analysis and processing tasks. In recent years, the field of natural image quality assessment has witnessed significant advancements. For example, the LIVE (LIVE Image and Video Quality Evaluation database) dataset, encompasses a diverse range of distorted images, each assigned subjective quality scores by professional human evaluators [8]. Moreover, numerous image quality metrics have been developed to evaluate various types of noise and distortions. These metrics include the Natural Image Quality Evaluator (NIQE) [9], the Perception-based

Image Quality Evaluator (PIQUE) [10], structural similarity (SSIM) [11], and Peak Signal-to-Noise Ratio (PSNR) [12]. However, in HSI, there is still a lack of specific human evaluators for the quality evaluation of individual bands. This presents a unique challenge in terms of data preprocessing.

Although some quality metrics are proposed for band-based individual images, they are mainly used in band selection and feature extraction in HSI. For example, Luo et al. [13] proposed an importance-assisted column subset selection (iCSBS) that uses an active gradient-reference index to evaluate the quality of each band and select the high-quality bands for further hyperspectral imaging. Cao et al. [14] introduced an objective image quality assessment combining the structural similarity index (SSIM) and mutual information to select the optimal band subset from the original hyperspectral data. Sun et al. [15] proposed a new HSI quality measuring index using noise-adjusted principal components and the Maximum Determinant of Covariance Matrix (MDCM) to find the bands with high signal-to-noise ratios (SNRs) and low correlation. Most studies focus on selecting the discriminative bands and only use them for further data analysis, discarding the rest of the bands. However, this results in the outright forfeiture of a substantial portion of spectral data. Recent research has unveiled the untapped potential and valuable information embedded within the water absorption bands [16, 17]. Besides, it is validated that these water absorption bands still contain useful information for data classification [6].

To mitigate the noise in low-quality bands of HSI, numerous researchers have devised sophisticated methodologies. For instance, Sun et al. [18] introduced an innovative technique called Fast Superpixel-based Subspace Low Rank Learning (FS2LRL) to solve the augmented Lagrangian method. After decomposing the initial HSI into two lower-rank sub-matrices, this method enforced the nuclear norm within superpixel-based regions to leverage the inherent spatial low-rank characteristics locally. Fan et al. [19] introduced an innovative denoising technique for HSI known as superpixel segmentation and low-rank representation (SS-LRR). Rather than using square patch as the conventional approach, this method opted for adaptive homogeneous regions. It subsequently applied the LRR to each of these homogeneous regions to effectively eliminate various types of noise simultaneously.

In recent years, deep learning methods have exhibited remarkable performance across various image restoration tasks. Sidorov et al. [20] proposed an effective single-HSI restoration algorithm, harnessing the intrinsic capabilities of a two-dimensional Convolutional Neural Network (CNN) (denoted as Deep-HS-prior 2D) without the necessity for training. Shi et al. [20] introduced a unique dual-attention HSI denoising network featuring separate branches for extracting spatial and spectral features, where a position attention module was employed for determining interdependencies within the feature map and a channel attention module for simulating spectral correlations. Additionally, a multiscale structure is then used to merge multiscale spatial and spectral features. Cao et al. [21] developed a deep spatial-spectral global reasoning network to consider both the local and global information for HSI noise removal. This new network can extract representations from new dimensions and help tackle complex noise by exploiting multiple representations.

These advanced HSI denoising methods leverage spectral, spatial, or high-level features to proficiently eliminate various types of noise. However, a significant limitation is that most of these methods are designed to introduce different specific types of simulated noises solely onto corrected HSI datasets (after pre-filtering the water absorption bands). In real scenarios, it is challenging to discern various noise categories, particularly within the water absorption bands in HSI, regardless the extra efforts that are needed for denoising before the reconstruction of the HSI.

For image reconstruction from noisy images, a number of models have been proposed. Some methods use the information from high-quality regions to fill in areas with lower quality, assuming similar statistical and geometrical structures within the neighbouring regions [22–25]. Additionally, auxiliary data was utilised to aid the image reconstruction, capitalising on the high correlation present among images [26, 27]. These studies have demonstrated promising results in reconstructing data for various satellite images. However, there remains a scarcity of research specifically targeting the reconstruction of low-quality bands within HSI.

In addition to the conventional approaches such as the Moving Average (MA) [28], Median Filtering (MF) [29] and Autoregressive Integrated Moving Average (ARIMA) [30], many signal processing tools have been utilised recently for data analysis, prediction and reconstruction, including Singular Spectrum Analysis (SSA) [31, 32], Long Short-Term Memory (LSTM) [33], Empirical Mode Decomposition (EMD) [34], and the Prophet model [6]. Herein, SSA, LSTM, EMD and Prophet have been successfully applied in HSI with validated efficacy in various tasks, such as feature extraction and classification even without prefiltering noisy water absorption bands [35]. As a recently developed forecasting tool by Facebook, the Prophet model has demonstrated its efficiency in analysing data as it can decompose data into several components, and further explore the different portions. Notably, the Prophet model can learn the trends and patterns from the observed data, making it robust and effective for the datasets with gaps, missing observations, and highly noisy data. HSI is characterised by sequential data in the spectral domain [18], encompassing intricate non-linear scattering noise and potential data gaps. Given these challenges, we are motivated to harness the capabilities of the Prophet model within the HSI context. Our objective is to leverage the Prophet model to reconstruct low-quality spectral bands using insights extracted from high-quality band images.

In this paper, we introduce a novel quality metric and band reconstruction method for HSI. Leveraging the Prophet model's exceptional ability to capture patterns from neighbouring bands, we achieve an effective reconstruction of low-quality bands, enabling the simulation of gradual transitions between bands. Our goal is to develop a comprehensive quality metric to model the complex noises in HSI and to facilitate the reconstruction of the discriminative features in low-quality

bands. The major contributions of this study are summarised as follows:

(1) The proposed quality metric takes into account spatial features on both local and global scales, as well as spectral features across neighbouring bands and the entire band spectrum. This enables it to effectively model complex noise and distortions present in HSI data.
(2) Notably, this work marks the first application of the Prophet model for band reconstruction in HSIs. The Prophet model adaptively predicts missing bands by leveraging the characteristics of neighbouring bands. These reconstructed bands prove highly beneficial for enhancing data analysis and facilitating HSI classification tasks.
(3) Combining the quality metric and the image reconstruction process, our proposed framework demonstrates its effectiveness in automating the preprocessing of HSI data.

This paper is structured as follows. Section 2 provides an introduction to the research background. In Section 3, we present a detailed description of the proposed framework. Section 4 covers the design of experiments, including information about the testing datasets, benchmarking methods and parameter settings. In Section 5, we present the experimental results and analysis. Finally, some concluding remarks are drawn in Section 6.

2 | BACKGROUND

2.1 | Concept and algorithm of the prophet model

Time series forecasting is a critical task in numerous domains, and the Prophet model [36], which is designed by Facebook, has emerged as a powerful tool for the analysis of time series data. Prophet has the ability of flexibility and accuracy when processing various time series data. The Prophet model can decompose the input data into several distinct components, each responsible for capturing specific aspects of the underlying patterns. As illustrated in Eq. (1), these components include the trend $g(t)$, seasonality $S(t)$, and holiday effects $f(t)$, and they are integrated into the model to provide a holistic understanding of the time series.

$$y(t) = g(t) + S(t) + f(t) + \varepsilon_t \tag{1}$$

where ε_t denotes an error term.

Trend modelling in the Prophet model is a vital component for capturing long-term patterns and changes in time series data. Prophet employs a piecewise linear approach, enabling it to handle intricate non-linear trends. The foundation for modelling the trend is the logistic growth function as shown below:

$$g(t) = 1/\left(1 + e^{-k(t-c)}\right) \tag{2}$$

where k determines the steepness of the trend growth, that is, the rate and c is an offset factor. In the Prophet model, we configure D changepoints across the entire time period t. At each changepoint, the growth rate is changed with δ_d ($\boldsymbol{\delta} \in \mathbb{R}^S$), which is calculated using a Laplace distribution: $\delta_d \sim$ Laplace (τ). Consequently, the growth rate at any changepoint is calculated by adding the rate adjustment to the previous growth rate.

$$k_d = k_{d-1} + \delta_d \tag{3}$$

Seasonality modelling is another integral aspect of the Prophet model. It aims to capture the recurring patterns and periodic fluctuations within the time series data. Seasonality is often decomposed into yearly, weekly, and daily components using Fourier series. The seasonality model can be defined as follows:

$$S(t) = \left[\cos\left(\frac{2\pi(1)t}{P}\right), \ldots, \sin\left(\frac{2\pi(L)t}{P}\right)\right]\boldsymbol{E} \tag{4}$$

where p denotes the period, such as the yearly or weekly cycle. The parameter E is computed using Normal $(0,\sigma^2)$. The parameter L determines the fitting performance of seasonality.

The Prophet model allows for the incorporation of holiday effects, enabling users to account for the impact of specific dates or periods on the time series. Holiday effects are introduced using binary indicators, indicating whether a date falls within a holiday period or not. These binary indicators take on a value of one if a particular date corresponds to a holiday and 0 otherwise. By including holiday effects in the model, Prophet allows for the explicit consideration of the unique characteristics associated with holidays, which may lead to deviations from regular time series patterns.

$$f(t) = V(t)\boldsymbol{\kappa} \tag{5}$$

where $V(t)$ is the binary indicator and $\boldsymbol{\kappa}$ is the magnitude of the effects caused by holiday events, where $\boldsymbol{\kappa}\sim$Normal $(0,\gamma^2)$.

2.2 | Non-reference image quality evaluator

Various methods assess image quality categorised as Full Reference, Reduced Reference, and No Reference. No Reference method can assess quality without any reference image [37]. Full and Reduced Reference methods are limited by the requirement for a perfect reference image, making No Reference methods more practical in real-world scenarios.

2.2.1 | Blind/referenceless image spatial quality evaluator

The Blind/Referenceless Image Spatial Quality Evaluator (BRISQUE) [37] is an exceptionally competitive No Reference

image quality assessment model. Given a grey image $I(i,j)$, the mean subtracted contrast normalised (MSCN) image $\hat{I}(i,j)$ is first calculated as follows:

$$\hat{I}(i,j) = \frac{I(i,j) - \mu(i,j)}{\sigma(i,j) + 1} \tag{6}$$

where $i = 1,\ldots,H$ and $j = 1,\ldots,W$ denote the spatial indices of an image. H and W are the image height and width, respectively. $\mu(i,j)$ and $\sigma(i,j)$ are the local mean and standard deviation calculated as follows:

$$\mu(i,j) = \sum_{m=-M}^{M} \sum_{n=-N}^{N} \omega(m,n) I(i+m, j+n) \tag{7}$$

$$\sigma(i,j) = \sqrt{\sum_{m=-M}^{M} \sum_{n=-N}^{N} \omega(m,n)[I(i+m,j+n) - \mu(i,j)]^2} \tag{8}$$

where $\omega = \{\omega(m,n) \mid m = -M,\ldots,M, n = -N,\ldots,N\}$ is a 2-dimension circularly symmetric Gaussian weighting function, sampled within 3 standard deviations ($M = N = 3$), and then scaled to unit volume.

In BRISQUE, the MSCN coefficients display varying behaviour with different distortions. To capture this diversity, these coefficients are modelled using a Generalised Gaussian Distribution (GGD), characterised by two key parameters: variance and shape of the distribution [38]. The adjacent pixels usually show homogeneity in the pristine image, disrupted in distorted images. Pairwise products of MSCN coefficients of neighbouring pixels are computed along horizontal, vertical, and diagonal orientations to capture this disruption: $\hat{I}(i,j)\hat{I}(i+1,j)$, $\hat{I}(i,j)\hat{I}(i,j+1)$, $\hat{I}(i,j)\hat{I}(i+1,j+1)$, and $\hat{I}(i,j)\hat{I}(i+1,j-1)$ then fitted in an Asymmetric Generalised Gaussian Distribution (AGGD) [39]. AGGD is characterised by four parameters: mean value, shape of the distribution, left-scale and right-scale parameter.

By extracting two parameters from the GGD and four parameters from the AGGD across four orientations, a total of 18 features are generated. Another 18 features are computed on a downsampled image (by a factor of 2), totalling 36 features to capture multiscale information. A Support Vector Machine Regressor (SVR) [40] is used to map these features into quality scores. The SVR is trained using both pristine reference images and distorted images with five types of distortions, each associated with a quality score. The LIBSVM package [41] served as a tool for implementing the Radial Basis Function (RBF) kernel SVR.

2.2.2 | Natural Image Quality Evaluator

The Natural Image Quality Evaluator (NIQE) is another competitive No-reference image quality index [9]. Different from BRISQUE, NIQE is not constrained by any distortion type.

First, the MSCN image $\hat{I}(i,j)$ is calculated following the same procedure in Eqs.(6)–(8) of BRISQUE. Then, the image is partitioned into square patches. Let these patches be indexed $b = 1,2,\ldots,B$, the local sharpness β in the bth patch is computed as follows:

$$\beta_b = \sum_{(i,j) \in patch\ b} \sum \sigma(i,j) \tag{9}$$

In NIQE, patches with $\beta > T_S$ are chosen, where T_S is set as a fraction ρ ($\rho = 0.75$) of the peak patch sharpness across the image. Following that, 36 features are extracted from each selected patch using GGD and AGGD, akin to the process in BRISQUE and subsequently modelled using the multivariate Gaussian (MVG) model.

Finally, for a test image, its quality is assessed by comparing its MVG fit to that of a set of pristine natural images, measuring the distance between the two.

$$Q^{Ni} = \sqrt{\left((\mu_{na} - \mu_{te})^T \left(\frac{\Sigma_{na} + \Sigma_{te}}{2}\right)^{-1} (\mu_{na} - \mu_{te})\right)} \tag{10}$$

where Q^{Ni} is the NIQE quality score of a test image, and μ_{na}, μ_{te} and Σ_{na},Σ_{te} denote the mean and covariance of the MVG for natural images and test image, respectively.

2.2.3 | Perception-based Image QUality Evaluator

The Perception-based Image Quality Evaluator (PIQUE) [10] is designed to estimate distortion exclusively within spatially prominent regions and at the local block level.

First, the MSCN coefficient $\hat{I}(i,j)$ is calculated and then divided into non-overlapping 16 × 16-sized blocks. These blocks are labelled as either Uniform (U) block or Non-uniform (NU) block as follows:

$$Block_b = \begin{cases} U & \nu_b < T_U \\ NU & \nu_b \geq T_U \end{cases} \tag{11}$$

where ν_b is the variance of the bth block, $b = 1,\ldots,B$. B is the total number of blocks. The threshold T_U is set to 10%.

Each edge of the NU blocks is segmented into 11 parts. A NU block is considered to exhibit noticeable distortion if any of its segments meets the following equation:

$$\sigma_{pq} < T_{STD} \tag{12}$$

where σ_{pq} is the standard deviation of the qth (where $q \in 1,2,\ldots,11$) segment in pth (where $p \in 1,2,3,4$) edge. T_{STD} is the threshold value, which is set to 10%.

Each *NU* block is also divided into two segments: the central and the surrounding segments. A block is considered affected by white noise if it meets the following criterion:

$$\sigma_b > 2 \times \frac{\left|\frac{\sigma_{cen}}{\sigma_{sur}} - \sigma_b\right|}{\max\left(\frac{\sigma_{cen}}{\sigma_{sur}}, \sigma_b\right)} \tag{13}$$

where σ_{cen} is the standard deviation of the central segment and σ_{sur} is the standard deviation of the surrounding segment. σ_b signifies the standard deviation of $Block_b$.

The PIQUE quality score Q^{Pi} of an image is calculated as follows:

$$Q^{Pi} = \frac{\left(\sum_{b=1}^{BN}\theta_b\right) + 1}{BN + 1} \tag{14}$$

where BN is the total number of *NU* blocks. θ_b quantifies the distortion in the bth *NU* block, which is computed as follows:

$$\theta_b = \begin{cases} 1 & if\ (12) and (13) \\ \nu_b & if\ (13) \\ 1 - \nu_b & if\ (12) \end{cases} \tag{15}$$

3 | THE PROPOSED APPROACH

The flowchart of the proposed approach is depicted in Figure 1, which has two main stages, that is, quality evaluation of HSI bands and band image reconstruction, as detailed in Figure 1.

3.1 | Quality evaluation for HSI bands

Different from the natural images, the noise in HSI data exhibits high spectral and spatial correlation, high dimensionality, randomness, and multiple sources of noise [35]. Therefore, it is difficult to distinguish the distortion categories in a band image. In this paper, a novel multi-scale and spectral-spatial image quality evaluator is proposed to comprehensively assess each band image in HSI. For a given HSI cube $\boldsymbol{I} \in R^{H \times W \times D}$ (where H, W, and D are the number of rows, columns and bands), the quality score of the dth band is calculated as follows:

$$Q_d = 1 - (Q_d^{Br} + Q_d^{Ni} + Q_d^{Pi} + Q_d^{Su} + Q_d^{PCA}) \tag{16}$$

where Q_d^{Br} is the BRISQUE score, Q_d^{Ni} is the NIQE score and Q_d^{Pi} is the PIQUE score. Q_d^{Su} stands for the superpixelwise quality score derived using the superpixel technique [6]. Q_d^{PCA} is extracted using the principal component analysis (PCA) [35] method, namely PCA loading quality evaluator in this study.

3.1.1 | No Reference Natural Image Quality Evaluator

The BRISQUE can evaluate band image quality in multiscale, which is particularly effective in capturing distortion categories in HSI band image including JPEG2000, JPEG, Gaussian blur, white noise, and a Rayleigh fast-fading channel simulation [37, 42]. For the dth band image I_d, its BRISQUE quality score Q_d^{Br} is calculated in multiscale with I_d and its downsampled image by half I_d'. The obtained 36 spatial features are mapped by SVR to the quality score.

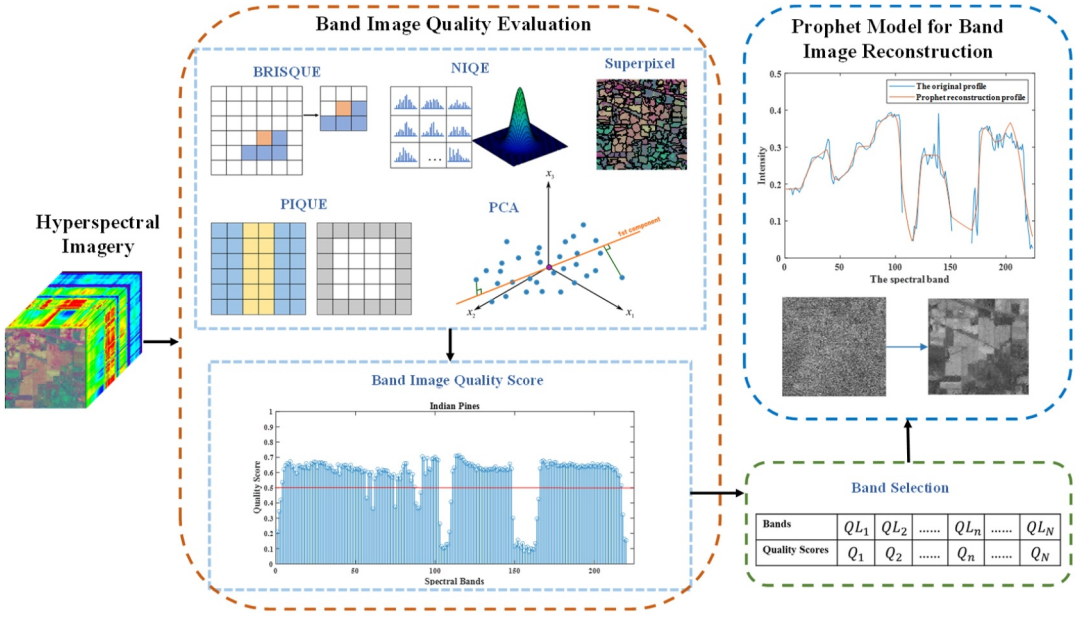

FIGURE 1 The flowchart of the proposed method.

NIQE can assess local distortions of each band image using block level spatial features. It offers the advantage of not being constrained by predefined categories of distortions [9], making it a versatile choice for evaluating the complicated distortions in HSI. Specifically, for a band image I_d, its MSCN is calculated and then partitioned into square blocks to extract the block level 36 spatial features. These features are fitted into an MVG model. The NIQE quality score Q_d^{Ni} is finally computed as follows:

$$Q_d^{Ni} = \sqrt{\left(\left(\mu_{na} - \mu_{I_d}\right)^T \left(\frac{\Sigma_{na} + \Sigma_{I_d}}{2}\right)^{-1} \left(\mu_{na} - \mu_{I_d}\right)\right)} \tag{17}$$

where μ_{na}, μ_{I_d} and $\Sigma_{na}, \Sigma_{I_d}$ represent the mean and covariance values of the MVG for natural images and the dth band image of HSI, respectively.

PIQUE can conduct a detailed spatial analysis of various sections and edges at the block level within HSI. For each band image, the block level distortion is estimated. The PIQUE quality score Q_d^{Pi} is calculated based on Eqs. (14–15).

3.1.2 | PCA loading quality evaluator

Q^{PCA} is proposed here as a quality evaluator by using the spectral information among the whole bands of HSI. PCA aims to discern the principal directions of variability inherent in the data and then project it from its original high-dimensional spectral space into a reduced-dimensional principal component space. These principal components contain the major features and patterns in the HSI dataset.

In the HSI cube, $\boldsymbol{I}$ denotes the $\boldsymbol{x}_p = [x_{p1}, x_{p2}, \ldots, x_{pD}]$ as one pixel vector in the cube (where $p \in [1, H \times W]$). Then, $\boldsymbol{x}_p$ is transformed as a mean-adjusted vector $\boldsymbol{z}_p$ as follows:

$$\boldsymbol{z}_p = \boldsymbol{x}_p - \frac{\mathbf{1}}{H \times W} \sum_{p=1}^{H \times W} \boldsymbol{x}_p \tag{18}$$

In order to identify the primary directions of variation within the data, the covariance matrix $\boldsymbol{C}$ is calculated:

$$\boldsymbol{C} = \mathrm{E}\left\{\left(\boldsymbol{x}_p - \mathrm{E}\{\boldsymbol{x}_p\}\right)\left(\boldsymbol{x}_p - \mathrm{E}\{\boldsymbol{x}_p\}\right)^T\right\} = \mathrm{E}\{\boldsymbol{z}_p \boldsymbol{z}_p{}^T\} \tag{19}$$

where $\mathrm{E}\{\bullet\}$ represents the mathematical expectation.

The matrix $\boldsymbol{C}$ can be presented as the multiplication of three matrices as follows:

$$\boldsymbol{C} = \boldsymbol{A}\boldsymbol{F}\boldsymbol{A}^T \tag{20}$$

where $\boldsymbol{F} = diag\ (\lambda_1, \lambda_2, \ldots, \lambda_D)$ denotes the diagonal matrix composed by the eigen values of $\boldsymbol{C}$, and $\mathbf{A}$ is the orthonormal matrix composed by the corresponding eigen vectors $[\boldsymbol{\alpha}_1, \boldsymbol{\alpha}_2, \ldots, \boldsymbol{\alpha}_D]$.

The uncorrelated vector $\boldsymbol{r}_p$ is finally derived through a linear transformation of the original pixel vector $\boldsymbol{z}_p$.

$$\boldsymbol{r}_p = \boldsymbol{A}^T \boldsymbol{z}_p = \begin{bmatrix} \alpha_{11} & \alpha_{12} & \cdots & \alpha_{1D} \\ \alpha_{21} & \alpha_{22} & \cdots & \alpha_{2D} \\ \vdots & & \ddots & \vdots \\ \alpha_{D1} & \alpha_{D2} & \cdots & \alpha_{DD} \end{bmatrix}_{D \times D} \begin{bmatrix} z_{p1} \\ z_{p2} \\ \vdots \\ z_{pD} \end{bmatrix}_{D \times 1} \tag{21}$$

It is validated that the first principal component represents the predominant direction in the data, encapsulating the maximum variance within the dataset. The first principal component r_{p1} is presented as follows:

$$r_{p1} = [\alpha_{11}\ \ \alpha_{12}\ \ \ldots\ \alpha_{1d}\ \ \ldots\ \ \alpha_{1D}]_{1 \times D} \begin{bmatrix} z_{p1} \\ z_{p2} \\ \vdots \\ z_{pD} \end{bmatrix}_{D \times 1} \tag{22}$$

where α_{1d} is also the loading factor, the weight of the original pixel vector to construct the principal component.

The loading factors describe the contributions of different bands in HSI to form the first component. Thus, the larger the value of α_{1d}, the greater the influence of the dth band hold on HSI data's structure and interpretation. In this paper, the loading factor value is used as another band image quality evaluator as follows:

$$Q_d^{PCA} = \alpha_{1d} \tag{23}$$

3.1.3 | Superpixelwise quality evaluator

NIQE and PIQUE make use of local block-level information in an image with a fixed window size. However, these blocks can often encompass pixels from various categories and edge regions, resulting in a significant variance within a block. This can have an impact on the accuracy of quality assessment on HSI with complicated scenes. In real-world scenarios, regions of interest are often characterised by irregular shapes and varying sizes [43]. Consequently, the statistical analysis of band image data at the block level should be tailored to the unique structures present in the image. In pursuit of this objective, this paper employs a superpixel technique [6] to delineate local homogeneous regions of differing sizes and shapes. In such a scheme, smoother areas tend to yield larger superpixels, while superpixels originating from more heterogeneous regions tend to be notably smaller. To be specific, the simple linear iterative cluster algorithm (SLIC) [44] is applied to obtain the superpixelwise segmentation of the HSI. SLIC is chosen for its

ability to achieve accurate boundary adherence while maintaining low computational complexity [45].

For a given HSI, the pseudo-colour image is firstly derived by applying PCA and extracting the first three components. Subsequently, the pseudo-colour image is transformed from the RGB colour space to the CIE-Lab colour space, where each pixel is represented by a 5-dimensional vector $\vartheta[l,m,n,h,w]$, comprising colour values (l,m,n), as well as spatial coordinates (h,w). Next, neighbouring pixels are systematically grouped into distinct clusters, known as superpixels. The specific process begins by evenly distributing b initial cluster centres across the image. Then, pixels are clustered within a square region of size 2R × 2 R, centred around these cluster centres, based on a homogeneity metric. The cluster centres are iteratively updated to the mean of the pixels within each cluster until they no longer shift. This results in the formation of well-defined superpixels within the image.

The homogeneity metric $\varphi(i,j)$ is defined as the combination of spectral distance and spatial distance to cluster adjacent pixels with spectral similarity into a single superpixel.

$$\varphi(i,j) = \sqrt{\left(Dist_{spe}\right)^2 + \frac{G}{R^2}\left(Dist_{spa}\right)^2} \tag{24}$$

where the parameter G is a geometric factor. $Dist_{spe}$ and $Dist_{spa}$ are the spectral distance and spatial distance, respectively, which are calculated as follows:

$$Dist_c = \sqrt{\left(l_j - l_i\right)^2 + \left(m_j - m_i\right)^2 + \left(n_j - n_i\right)^2} \tag{25}$$

$$Dist_s = \sqrt{\left(h_j - h_i\right)^2 + \left(w_j - w_i\right)^2} \tag{26}$$

Next, the quality of each individual band image in HSI is assessed at the superpixel level. The location indices of all pixels within each superpixel are recorded and mapped to all the spectral bands, resulting in non-overlapping 3-D superpixels [43]. Here, the standard deviation is utilised, which is capable of quantifying local image sharpness. For the dth band image, its superpixelwise quality score Q_d^{Su} is computed as the average of the standard deviations across all superpixels.

$$Q_d^{Su} = \frac{1}{B}\sum\nolimits_{b=1}^{B}\sigma_{b,d} \tag{27}$$

where $\sigma_{b,d}$ is the standard deviation of bth superpixel for the dth band image.

3.2 | Band image reconstruction via prophet model

In this section, we initiate the process by identifying low-quality bands through a thresholding selection strategy based on their quality scores, Q_d. Specifically, if a band's quality score is lower than T_Q, then it is selected.

$$I_d \in \boldsymbol{QL} \quad if\ Q_d < T_Q \tag{28}$$

where $\boldsymbol{QL}$ is the low-quality bands set. Subsequently, these identified low-quality bands are excluded from the HSI dataset and undergo a reconstruction process using the Prophet model.

From section 2.1, it is clear that the Prophet model employs a logistic growth curve to capture trends in time series data, which allows for more complex non-linear patterns in the data. It incorporates the direction, the change rate and curvature of trends, which enables it to adaptively adjust the shape of the trend curve to better fit the data. Based on Eqs. (1–3), it is evident that the derived trend component, $g(t)$, is not solely reliant on the isolated observation at a single time point, t. Instead, it also incorporates information from other time points. This characteristic imparts a degree of resilience to $g(t)$ against noise fluctuations and the presence of missing data. Consequently, the Prophet model holds great potential for the analysis and processing of the low-quality band images in the uncorrected HSI dataset.

The HSI also characterises sequential data, albeit in the spectral domain [28]. The spectral intensity value of each pixel changes across multiple contiguous bands. This unique nature of HSI data motivated us to apply the Prophet model for the analysis and reconstruction of low-quality bands. It is challenging to apply periodic seasonality settings to encapsulate the complex, non-periodic variations in HSI. In this study, only the trend component is used as recommended in ref. [6]. Specifically, if I_d is recognized as a low-quality band, for the ith pixel in I_d, the reconstructed intensity value is computed as follows:

$$x_{i,d}^R = C_i / \left(1 + e^{-k_d(d-c_d)}\right) \tag{29}$$

where C_i denotes the carrying capacity of the ith pixel, adaptively determined by considering the input spectra. It is defined as the maximum value observed among all the spectra across different bands, mathematically represented as $C_i = \max\limits_{d\in\{1,\ldots,D\}} x_{i,d}^R$.

To more effectively capture the statistical spectral-spatial structures within a HSI across all bands, we designate each individual band as a changepoint. This approach facilitates the identification of local spectral transitions between consecutive bands, aiding in the construction of a band image. Based on Eqs. (1)–(3), k_d and c_d in an HSI data can be calculated.

Figure 2 displays the reconstruction results for the low-quality bands using the Prophet model. To illustrate the performance, a single pixel from the Salinas dataset [40] is focused on. In Figure 2a, we observe that the Prophet model successfully predicts and restores the removed low-quality bands, utilising trend modelling that takes into account information from neighbouring bands. Figures 2b and c clearly demonstrate the impressive performance of the Prophet model in low-quality band reconstruction. It is evident that the reconstructed image in Figure 2c exhibits well-defined structural and edge details, along with clear and discernible content.

4 | EXPERIMENTAL SETTINGS AND DATASETS DESCRIPTION

In this study, three publicly accessible HSI datasets for performance evaluation are utilised. The datasets and the specifics of our experimental settings are elaborated below.

4.1 | Description of the datasets

The first dataset employed in our study is the Indian Pines dataset, obtained through the Airborne Visible/Infrared Imaging Spectrometer (AVIRIS) sensor [46]. This dataset hails from the scenic Indian Pines study region in Northwest Indiana, USA, featuring a 145 × 145 pixel grid with a spatial resolution of 20 m per pixel. It encompasses a remarkable 220 spectral bands, spanning wavelengths from 0.4 to 2.5 μm. In this dataset, there are 20 water absorption bands (104–108, 150–163, and 220). The dataset is characterised by its diversity of land-cover classes, numbering 16 in total, with a predominant focus on various crop types. This diversity makes it a valuable asset for tasks spanning agricultural monitoring, land-use classification, and hyperspectral image analysis.

Our second dataset is the Salinas, acquired again by the AVIRIS sensor [46]. It was meticulously collected in the picturesque Salinas Valley, nestled within the scenic landscapes of California, USA. The dataset unfolds with an expansive canvas of 512 × 217 pixels, each representing an area of 3.7 m per pixel. The Salinas dataset features a grand total of 224 spectral bands with 20 water absorption bands (108–112, 154–167, and 224). Its ground truth map includes 16 distinct land-cover classes, including vegetables, bare soils, and vineyard fields.

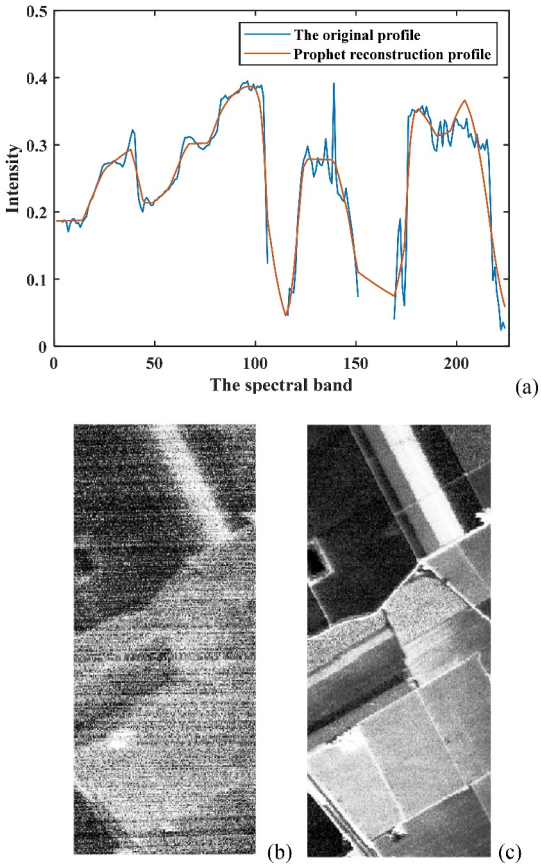

FIGURE 2 The Prophet reconstruction results. (a) The reconstructed profile by the Prophet model. (b) The original first band in the Salinas dataset. (c) The reconstructed image of (b) using the Prophet model.

4.2 | Experimental settings

The comparison analysis was conducted and benchmarked with six band denoising and reconstruction methods, including moving average (MA) [28], median filtering (MF) [29], autoregressive integrated moving average (ARIMA) [30], two dimensional Deep Hyperspectral prior (Deep-HS-prior 2D) [20], superpixel segmentation-based denoising (SS-LRR) [19] and fast superpixel-based subspace low-rank learning method (FS^{2}LRL) [18]. Note that the methods MA, MF, ARIMA and Prophet are merely based on the spectral information for reconstruction, while the SS-LRR, FS^{2}LRL and Deep-HS-prior 2D are spatial-spectral reconstruction methods. These comparing methods are used to generate reconstructed images for the selected low-quality bands. In MF and MA, to balance stability and accuracy, the window size is set to 5. In ARIMA, the number of lag observations, the number of times differencing, and the size of the moving average window are empirically set to 3, 1, and 1, respectively. In SS-LRR, the superpixel number is set to 40 for Indian pines and Salinas dataset, and 190 for PaviaU dataset. In FS^{2}LRL, the subspace dimension, superpixel number, sparse parameter and fidelity parameter are set to 10, 100, 0.13 and 0.040, respectively, for all datasets. The Deep-HS-prior 2D uses the Leaky Rectified Linear Unit (LeakyReLU) as the activation function, bilinear method for upsampling and adaptive moment estimation (ADAM) for optimisation. In Prophet, based on the parameter analysis in ref. [6], the scale parameter τ is set to 20. Other parameters for the comparing approaches are configured based

TABLE 1 List of parameter settings for our proposed MSPM framework and other benchmarking approaches.

Method	Settings
MF	Window size: 5
MA	Window size: 5
ARIMA	Number of lag observations: 3; Number of times differencing: 1; Size of the moving average window: 1
SS-LRR	Superpixel number: Indian Pines/Salinas (40), PaviaU (190)
FS^{2}LRL	Subspace dimension: 10; superpixel number: 100; Sparse parameter: 0.13; fidelity parameter: 0.040
Deep-HS-prior 2D	Activation function: LeakyReLU; upsampling method: Bilinear; optimisation method: ADAM; filter: 3 × 3
Prophet	τ:20; r_0:0; m_0:0

on their recommended default values, as detailed in Table 1. The experiments are also applied on the original HSI profile as a baseline. Note that all involved methods use the same low-quality band selection strategy. Here, for the superpixelwise quality evaluator, the segmentation scales for Indian Pines, Salinas and PaviaU are set to 100, 600 and 200, respectively, which are validated as the optimal settings in ref. [6].

To evaluate the performance of the proposed method, we have conducted three sets of experiments. The first set of experiments shows the outcomes of selecting low-quality bands across different datasets, validating the effectiveness of our quality-based band selection strategy.

The second set aims to provide a quality evaluation of the reconstructed band images. This employs various quality indices, including root-mean-square error (RMSE), structural similarity (SSIM) [11], Peak Signal-to-Noise Ratio (PSNR) [12], and the relative dimensionless global error in synthesis (ERGAS) [47]. Here, the reference image I^{ref} is derived from the median image of the HSI cube. This specific image has been validated that it can sufficiently encapsulate the properties of the entire dataset [48].

$$I^{ref} = \text{Median}\,(I_1, I_2, \ldots, I_D) \tag{30}$$

The RMSE (MRMSE) is used as the average pixelwise similarity between all reconstructed low-quality bands and the reference image:

$$\text{MRMSE}\left(\boldsymbol{QL^R}, I^{ref}\right) = \frac{1}{N}\sum_{n}^{N}\text{RMSE}\left(QL_n^R, I^{ref}\right) \tag{31}$$

where $\boldsymbol{QL^R}$ is the reconstructed bands in set $\boldsymbol{QL}$, and N is the number of low-quality bands. The RMSE is calculated as follows:

$$\text{RMSE}\left(QL_n^R, I^{ref}\right) = \sqrt{\frac{\sum_{p=1}^{H\times W}\left\|QL_{n,p}^R - I_p^{ref}\right\|_2}{H\times W}} \tag{32}$$

where $p \in [1, H \times W]$ is the index of the pixel in one band image. The RMSE is a commonly employed metric for quantifying the disparity between two images through the evaluation of pixelwise discrepancies. When the RMSE value approaches zero, it indicates that the reconstructed image closely resembles the reference image.

The mean SSIM (MSSIM) is given by

$$\text{MSSIM}\left(\boldsymbol{QL^R}, I^{ref}\right) = \frac{1}{N}\sum_{n}^{N}\frac{\left(2\mu_{QL_n^R}\mu_{I^{ref}} + \epsilon_1\right)\left(2\sigma_{QL_n^R, I^{ref}} + \epsilon_2\right)}{\left(\mu_{QL_n^R}^2 + \mu_{I^{ref}}^2 + \epsilon_1\right)\left(\sigma_{QL_n^R}^2 + \sigma_{I^{ref}}^2 + \epsilon_2\right)} \tag{33}$$

where μ and σ denote the mean value and standard deviation, respectively. ϵ_1 and ϵ_2 are two constants. SSIM compares local pixel intensity patterns between two images, yielding values between 0 and 1. A value of 1 signifies identical reference and reconstructed images.

The MPSNR is calculated as follows:

$$\text{MPSNR}\left(\boldsymbol{QL^R}, I^{ref}\right) = \frac{1}{N}\sum_{n}^{N}\left(20\times\log_{10}MAX_I - 10\times\log_{10}\text{RMSE}\left(QL_n^R, I^{ref}\right)^2\right) \tag{34}$$

where MAX_I represents the maximum possible range of pixel values. In this study, $MAX_I = 255$. A higher PSNR value indicates a higher similarity between the two images and lower image quality loss.

The ERGAS is defined as follows:

$$\text{ERGAS}\left(\boldsymbol{QL^R}, I^{ref}\right) = \frac{100}{u}\sqrt{\frac{1}{N}\sum_{n}^{N}\frac{\text{RMSE}\left(QL_n^R, I^{ref}\right)}{\mu_{I^{ref}}^2}} \tag{35}$$

where u is the spatial downsampling factor. ERGAS assesses image quality based on the normalised average error in each band. Higher ERGAS values signal image distortion, while lower values indicate greater similarity to the reference image.

The third experiment evaluates classification performance after reconstructing low-quality bands. To circumvent any potential confounding effects arising from the choice of the classifier itself, we have opted for the simplest classifier, namely K-Nearest Neighbours (KNN) [32, 49]. To ensure a fair classification comparison with the more advanced spatial-spectral methods, particularly due to the exclusive reliance of the proposed Prophet reconstruction method on spectral information, we have introduced a spatial augmentation technique. This involves employing a majority voting strategy with a 3 × 3 window size within the classification map. This enhancement effectively integrates spatial details into the Prophet method, which is denoted as PMV in this paper. To mitigate random variations and mitigate potential systematic errors, we performed 10 independent runs for all experiments. In each run, we employed a random partitioning of the training and testing sets, ensuring there was no overlap. More specifically, we adopted a stratified sampling strategy, allocating a training sample size of 10% for each distinct land cover class. For the quantitative evaluation of classification performance, the metrics including Overall Accuracy (OA), Kappa coefficients (κ), and Average Accuracy (AA) are employed.

All experiment sets were implemented using the Matlab 2023a platform on a computer with an 11th Gen Intel(R) Core (TM) i9-11950H (2.61 GHz) and 32.0 GB of memory. The Prophet model was implemented on the Python 3.8.16 with CUDA 11.7.

5 | EXPERIMENTAL RESULTS

In this section, a comprehensive qualitative and quantitative evaluation in four sets of experiments is reported to validate the efficacy of the proposed approach.

5.1 | Results of band selection

The obtained band-wise quality scores from the two datasets are visualised in Figure 3, with the threshold value T marked as a red line. The histograms of the band quality score of these two datasets are also given in Figure 4. It is evident from Figure 3 that there are low-quality bands in each dataset. In the Indian Pines dataset as shown in Figure 3a, the majority of bands have a quality score below 0.7, and their scores tend to cluster within the range of 0.6–0.7, as also being validated in Figure 4a. For the Salinas dataset shown in Figure 3b, band quality scores lie mainly in the range of 0.6–0.8. When it comes to the low-quality bands, it is noteworthy that Indian Pines has the lowest quality scores. As seen in Figure 4, the quality scores for the low-quality bands in Indian Pines are predominantly within the range of 0.1–0.2, whereas for the Salinas dataset, they cluster around 0.3–0.4. These results validate that Indian Pines exhibits the lowest band quality.

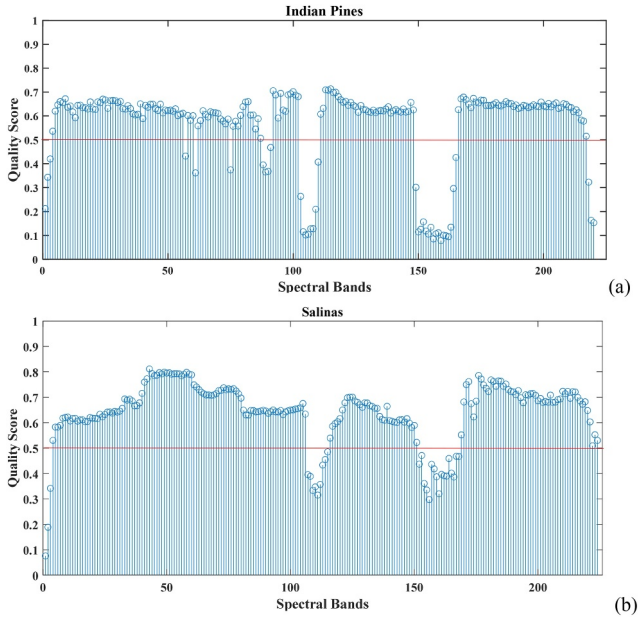

FIGURE 3 The quality score of each band in three datasets. (a) Indian Pines dataset and (b) Salinas dataset.

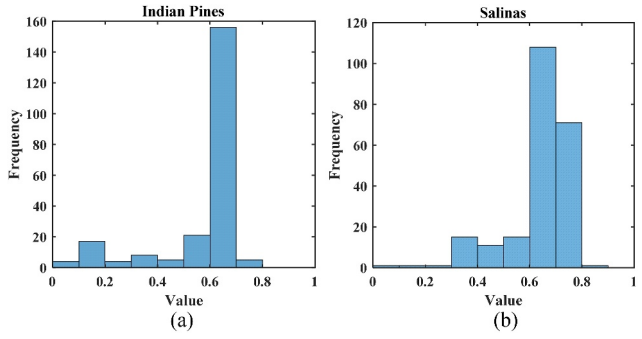

FIGURE 4 The histogram of the band quality score. (a) Indian Pines dataset and (b) Salinas dataset.

By adopting the thresholding selection strategy, the low-quality bands with the quality score lower than T are selected as presented in Table 2. Note that the low-quality bands are listed in the ascending order of their quality. As shown, in total, we have 38 and 29 low-quality bands selected from the Indian Pines dataset and Salinas dataset, respectively. The water absorption bands in the Indian Pines dataset (104–108, 150–163, and 220) and Salinas dataset (108–112 and 154–167) are successfully selected by our proposed method. This affirms the effectiveness of the proposed HSI quality evaluator in successfully identifying bands characterised by higher noise levels and a lesser content of useful information. It is worth noting that in addition to the water absorption bands, certain low-quality bands have also been selected. Intriguingly, these selected bands exhibit even greater noise levels and a more limited quantity of valuable information compared to the water absorption bands. These bands, therefore, wield a considerable effect on the subsequent data analysis including classification. However, a predominant portion of existing research tends to exclusively remove water absorption bands during the data pre-processing stage.

Figure 5 displays band images in the Salinas dataset for the first 224th (water absorption band) and 43rd bands. As seen in Figure 2, it is evident that even the first band, despite not being a water absorption band, exhibits higher levels of noise and less useful content compared to the 224th band. Therefore, it is necessary to process this band as well. The 43rd band, which has been selected as the highest quality band in the Salinas

TABLE 2 The bands selected by the proposed method.

Dataset	Low-quality bands
Indian Pines	159, 156, 162, 161, 160, 105, 106, 154, 157, 158, 150, 104, 153, 151, 107, 108, 155, 163, 220, 152, 219, 109, 1, 103, 164, 149, 218, 2, 61, 89, 90, 75, 88, 110, 3, 165, 57, 91
Salinas	1, 2, 156, 111, 160, 109, 155, 3, 110, 112, 154, 166, 159, 108, 163, 162, 107, 161, 165, 158, 113, 157, 152, 114, 164, 168, 167, 153, 115

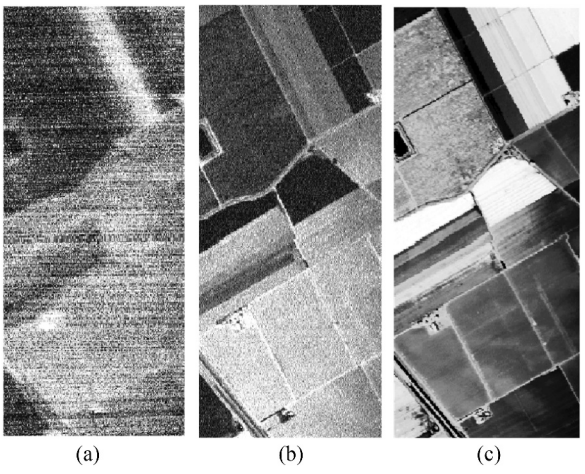

FIGURE 5 The band images in the Salinas dataset. (a) The first band, (b) The 224th band (water absorption band), and (c) The 43rd band.

dataset, displays evident structural features, sharp edges, and intricate details.

To sum up, the proposed algorithm can accurately identify low-quality bands with limited useful content and noise.

5.2 | Results of band quality assessment

The qualities of the reconstructed bands by different comparing methods are first assessed based on quality indices, which include MRMSE, MSSIM, MPSNR, and MERGAS. The summarised quantitative results from two datasets are presented in Table 3. The best-performing results are highlighted in bold, while the second-ranking results are marked with underlines. The visual reconstruction results of low-quality band images are also provided to check and assess the fidelity and perceptual quality of the image restoration process. These results serve as a crucial means of evaluating the effectiveness of the restoration technique and ensuring that the reconstructed images meet the desired standards of clarity and visual appeal.

5.2.1 | Quantitative results

As depicted in Table 3, the Prophet model exhibits the most favourable outcomes in terms of quality indices for reconstructing low-quality bands when compared to alternative methods across all datasets. The Prophet model consistently achieves the top results in MRMSE, MPSNR, and MERGAS indices across all datasets.

The Indian Pines dataset suffers from significant corruption due to water absorption and noise factors [18]. Leveraging the predictive capabilities of the Prophet model results in substantial enhancements in image quality. Specifically, there is a noticeable increase of 0.0694 in MRMSE, 0.3132 in MSSIM, 4.3889 in MPSNR, and 181.4719 in MERGAS when compared to the baseline. While the spectral reconstruction methods MF, MA, and ARIMA methods also contribute to noise reduction and image quality improvement, their effectiveness falls short when compared to the spatial-spectral methods including Deep-HS-prior 2D, SS-LRR and FS^{2}LRL. Remarkably, the SS-LRR model achieves the highest MSSIM result and consistently ranks second in most cases on the Indian Pines dataset. MSSIM, a metric index, assesses image similarity by comparing their structural similarities. Consequently, approaches considering spatial features often yield superior MSSIM values. Despite being a spectral method, the Prophet model also attains competitive results in the MSSIM metric.

On the Salinas dataset, the proposed Prophet model notably enhances the quality of low-quality bands. Compared to the baseline, the Prophet model demonstrates significant improvements across multiple metrics: an increase of 0.1143 in MRMSE, 0.5677 in MSSIM, 5.6053 in MPSNR, and 356.242 in MERGAS. Additionally, the deep learning method, Deep-HS-prior 2D, outperforms SS-LRR on this dataset, securing the top rank in MSSIM. This validates the efficacy of deeper feature extraction on the Salinas dataset. Simultaneously, experiments conducted on two different datasets indicate that simple spectral methods exhibit competitive performance in quality indices as observed in MA.

5.2.2 | Visual results

Figure 6 presents an example illustrating the visual reconstruction performance of various methods applied to the Indian Pines dataset. Due to the influence of water absorption effects, the 150th band suffers from significant information loss and appears visually inundated with noise, devoid of useful information. Through different reconstruction techniques, as evident in Figures 6 b–h, these methods are capable of removing a substantial amount of noise and reconstructing the structural information of objects within the scene. As depicted in Figures 6b–d, spectral methods including MF, MA, and ARIMA utilise data from adjacent bands to restore valuable information within the low-quality bands. However, these methods still exhibit some noise due to the absence of spatial information utilisation. Notably, the MA method produces a visually improved result, presenting a smoother reconstructed scene compared to MF and ARIMA. This observation aligns

TABLE 3 The quality indices of the reconstructed bands using different methods for two datasets (Bold = Best, underline = second-best).

	Indian Pines				Salinas			
Methods	**MRMSE↓**	**MSSIM↑**	**MPSNR↑**	**MERGAS↓**	**MRMSE↓**	**MSSIM↑**	**MPSNR↑**	**MERGAS↓**
Baseline	0.1850	0.1868	15.0913	483.7387	0.2542	0.1036	11.9845	791.9360
MF	0.1561	0.3212	16.7475	408.1868	0.2500	0.1240	12.2872	778.7319
MA	0.1465	0.3703	17.3392	383.0707	0.2447	0.1672	12.3939	762.3666
ARIMA	0.1806	0.2594	15.2956	472.3751	0.2617	0.1072	11.5859	815.2262
SS-LRR	0.1405	**0.5925**	17.8063	364.1436	0.2525	0.1517	12.0981	786.6938
FS^{2}LRL	0.5174	0.3470	6.0979	1348.0000	0.2627	0.1226	11.6502	812.1584
Deep-HS-prior 2D	0.1737	0.3906	15.5604	465.3076	0.1415	**0.6743**	16.8898	440.9015
Prophet	**0.1156**	0.5000	**19.4802**	**302.2668**	**0.1399**	0.6713	**17.5898**	**435.6940**

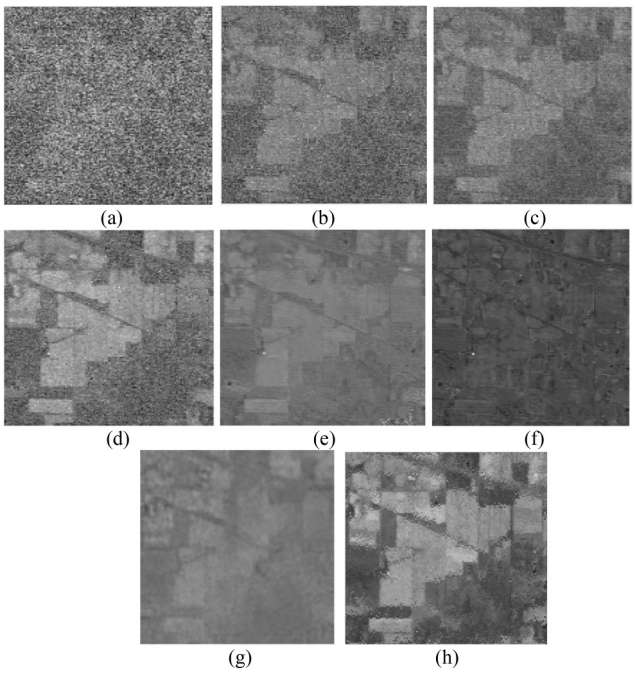

FIGURE 6 The visual reconstruction performance of different methods on the Indian Pines dataset. (a) The 150th band, and the result from (b) MF, (c) MA, (d) ARIMA, (e) SS-LRR, (f) FS^{2}LRL, (g) Deep-HS-prior 2D and (h) the proposed Prophet model.

with the quantitative findings outlined in Table 3. The spatial-spectral approaches SS-LRR, FS^{2}LRL, and Deep-HS-prior 2D depicted in Figure 6e–g effectively eliminate noise, presenting significantly smoother and clearer boundaries compared to spectral methods. Particularly, in Figure 6g, Deep-HS-prior 2D produces the smoothest reconstructed scene among all methods compared. The proposed method, the Prophet model in Figure 6f functioning as a spectral method, when contrasted with spatial-spectral algorithms, it yields a less smooth reconstructed scene. However, it still retains crisp outlines and boundaries of objects and can even capture finer details within objects. Moreover, the proposed method exhibits more pronounced distinctions between different categories in the reconstructed images, indicating its significant preservation of discriminative information among various classes. This underscores the superior performance of the Prophet model in the domain of image reconstruction.

5.3 | Results of HSI data classification

In this section, our objective is to validate the efficacy of reconstructing low-quality spectral bands. This process not only serves to enhance the quality of these bands by reducing noise and accentuating pertinent land cover features, but it also facilitates more in-depth data analysis and classification. Our primary goal is to ascertain whether employing different reconstruction algorithms confers advantages in the classification of diverse HSI scenes characterised by the presence of low-quality spectral bands.

5.3.1 | Results from the Indian Pines dataset

Table 4 presents the classification results obtained using various low-quality band image reconstruction methods, with a training sample size of 10%, on the Indian Pines dataset. It is evident that utilising the original low-quality bands yields a low classification accuracy, with an Overall Accuracy (OA) of 61.3465%. However, employing spectral reconstruction methods, such as MF, MA, and ARIMA, has led to some improvements in classification results. Notably, the proposed Prophet model achieved the highest OA, Kappa, and AA among all spectral methods, showcasing a notable increase of 9.7032% in OA compared to the baseline. Moreover, the incorporation of spatial features in spatial-spectral methods including SS-LRR, FS^{2}LRL, and Deep-HS-prior 2D, significantly enhanced the classification performances. SS-LRR demonstrated the highest OA among all methods considered, exhibiting an increase of 18.4542% in OA compared to the baseline. It is worth noting that while FS^{2}LRL demonstrates moderate performance in the quality indices comparison within Section 5.2, it notably outperforms spectral methods in classification tasks. This occurrence primarily arises from the Indian Pines dataset's scene containing numerous block-like regions, where the definition by Ground Truth (GT) is coarse. Spatial features can reduce differences within these blocks, leading to more meaningful classifications. On the contrary, the spectral reconstruction methods can preserve substantial detailed information. When we integrate spatial features into the Prophet model (PMV), classification results experience further enhancement. PMV achieves the best Kappa and AA on the Indian Pines dataset, showing competitive OA results akin to SS-LRR.

When examining individual class-based performance, the PMV demonstrates the highest classification accuracy in 10 out of 16 classes. Taking the second position is Deep-HS-prior 2D, which excels in achieving the best results for 4 classes. In summary, the proposed Prophet model, despite being a spectral reconstruction method, exhibits competitive performance in classification tasks compared to spatial-spectral methods. Particularly, when incorporating simple spatial features, known as the PMV algorithm, it demonstrates excellent classification results, surpassing advanced spatial-spectral methods in many class-based results. These results unequivocally demonstrate the effectiveness of Prophet's image reconstruction for HSI classification, primarily attributable to its exceptional ability to accurately capture features from the spectral bands, even in the presence of missing data and noise interference. Prophet employs non-linear models and leverages available data points to fit trends as accurately as possible.

5.3.2 | Results from the Salinas dataset

As for the Salinas dataset, in contrast to the Indian Pines, it presents a different set of challenges and characteristics. It exhibits notably lower susceptibility to significant noise interference, resulting in clearer and more distinct scenes within the

TABLE 4 Classification accuracy (%) of all involved methods on the Indian Pines dataset with 10% training samples per class (Bold indicates the best results).

Class	Baseline	MF	MA	ARIMA	SS-LRR	FS^{2}LRL	Deep-HS-prior 2D	Prophet	PMV
1	8.8095	14.7619	20.0000	17.8571	22.381	22.619	**26.6667**	22.8571	18.5366
2	55.2255	59.3468	60.5988	62.5350	75.6687	68.6936	78.1571	65.9409	**80.1400**
3	39.0361	45.5154	48.2865	44.9799	**67.925**	59.17	64.7523	51.4324	56.3855
4	23.1776	29.8598	24.7664	27.8972	35.7009	36.1215	**38.1308**	32.8972	37.9907
5	71.4023	76.2529	81.6322	70.1839	87.7471	84.092	87.5632	78.4828	**89.7471**
6	93.3790	95.5099	95.9513	92.2527	97.382	96.0274	97.0472	96.0426	**99.6347**
7	18.4615	29.2308	46.5385	62.3077	65.7692	59.2308	68.0769	49.2308	**96.0870**
8	97.7494	98.2135	97.5638	96.9374	99.0255	98.6775	99.7216	98.6079	**99.8376**
9	5.5556	5.0000	8.3333	0	12.2222	6.1111	10	6.6667	**34.6667**
10	41.6114	49.9086	56.0686	50.0343	82.7771	75.5886	**83.8743**	66.6286	83.0629
11	66.2127	68.4299	70.8643	64.0045	86.2579	79.8416	83.1312	77.3032	**86.5928**
12	20.8989	26.1798	28.3333	26.3670	**51.573**	43.015	47.2097	36.0300	43.9700
13	90.3243	90.1622	91.4054	89.6757	97.0811	94.2703	95.027	88.4324	**98.3243**
14	90.0527	90.9921	90.6409	89.0781	92.1422	93.3099	95.8648	91.5364	**97.7524**
15	15.8908	18.3046	18.4483	16.7241	36.2931	25.7471	**37.5**	21.6667	13.8506
16	82.7381	83.3333	83.0952	83.5714	84.6429	84.5238	83.9286	82.8571	**90.2381**
OA	61.3465	64.8900	66.7804	63.4254	**79.8007**	74.7925	79.5288	71.0497	79.5523
κ	0.5550	0.5965	0.6185	0.5806	0.7687	0.7111	0.7656	0.6676	**0.7711**
AA	51.2828	55.0626	57.6579	55.9004	68.4118	64.19	68.5407	60.4133	**70.4261**

spectral data. Hence, the level of spectral mixture is less severe as observed in the Indian Pines dataset. As a result, the incorporated spatial features failed to yield significant improvements as observed in the Indian Pines dataset. As shown in Table 5, the spatial-spectral methods did not notably improve the classification results when compared against the baseline and spectral methods.

The proposed Prophet model, functioning as a spectral reconstruction method, exhibits a higher OA compared to FS^{2}LRL and slightly lower performance than SS-LRR and Deep-HS-prior 2D. The Prophet model shows an increase of 1.6313% in OA over the baseline. Upon the inclusion of spatial features into the Prophet model, namely PMV, it achieves the highest scores in terms of OA, κ, and AA. Specifically, the OA surpasses the baseline by 5.4975% and outperforms the advanced deep learning method Deep-HS-prior 2D by 2.9356%.

Furthermore, when delving into individual class-based classification performance, PMV demonstrated exceptional results. It attained optimal classification values for a range of scenarios, particularly excelling in the classification of 12 distinct classes and an expansive set of 16 land cover categories. Notably, the Deep-HS-prior 2D algorithm also displayed noteworthy performance, emerging as the leader in the classification of 2 specific classes within the Salinas dataset. These findings underscore the versatility and effectiveness of our proposed algorithm across varying classification scenarios within the Salinas dataset, ultimately positioning it as a robust choice for hyperspectral image classification tasks.

6 | CONCLUSION

Our study introduces a robust and innovative framework for the quality assessment and the reconstruction of HSI bands. Firstly, we have validated the effectiveness of our proposed quality metric, which utilises spatial-spectral features at both global and local scales. This metric has demonstrated its capability to accurately model complex and distorted bands, resulting in the selection of water absorption bands and noisy bands across all datasets. Secondly, the Prophet model, leveraging features and trends from neighbouring high-quality bands, has exhibited remarkable effectiveness in reconstructing low-quality bands with enhanced structural clarity and details. After conducting comprehensive experiments on two publicly available uncorrected datasets, our findings unequivocally establish the superior performance of our proposed framework in reconstructing low-quality bands into high-quality ones compared to state-of-the-art spectral and spatial-spectral band reconstruction algorithms. Additionally, our results showcase that the reconstructed images produced by our proposed method attain competitive and promising classification

TABLE 5 Classification accuracy (%) of all involved methods on the Salinas dataset with 10% training samples per class (Bold indicates the best results).

Class	Baseline	MF	MA	ARIMA	SS-LRR	FS^{2}LRL	Deep-HS-prior 2D	Prophet	PMV
1	97.8994	98.3029	98.4577	**98.8004**	98.7231	98.4467	98.607	98.0763	98.1758
2	99.4574	99.5081	99.5558	99.5021	99.5319	99.4723	99.4097	99.3560	**99.9046**
3	98.9039	99.3479	99.4604	99.4379	99.6402	99.4885	99.5559	99.4941	**100.0000**
4	99.4343	99.4821	99.4422	99.4661	99.5697	99.5378	99.498	99.4900	**100.0000**
5	97.4326	97.7934	97.9428	98.1958	98.3078	97.8847	97.9469	98.1253	**99.0875**
6	99.6493	99.7278	99.6605	99.7306	99.6633	99.697	99.6829	99.7194	**100.0000**
7	99.4134	99.4475	99.3048	99.3979	99.3886	99.4693	99.4382	99.4724	**99.9286**
8	77.0584	78.8437	78.6731	79.7250	80.5816	79.8571	78.3498	79.3849	**91.5103**
9	99.3337	99.2907	99.4358	99.2764	99.4698	99.3785	99.5236	99.4519	**99.8155**
10	89.2918	90.3253	90.9929	91.5825	92.1484	91.0505	92.3517	92.1721	**95.5981**
11	92.9522	95.7277	94.9480	95.7588	95.9979	95.9356	96.1954	95.7796	**97.8274**
12	99.2219	99.5562	99.6427	99.7579	99.781	**99.8329**	99.6945	99.6772	98.9164
13	97.6121	97.8182	97.6121	97.3939	97.6364	97.4424	97.5636	97.4788	**98.7636**
14	92.6687	93.0737	92.5961	93.6033	93.1672	93.3022	93.4787	92.3157	**96.8640**
15	59.5460	62.2164	62.7866	64.3335	65.5564	65.0168	**73.6487**	64.2158	72.2516
16	97.2711	97.5722	97.5046	97.5476	97.6521	97.4063	**97.8242**	97.3694	94.8986
OA	88.2629	89.2008	89.2766	89.7911	90.2038	89.8615	90.8248	89.8942	**93.7604**
K	0.8692	0.8797	0.8806	0.8863	0.8909	0.8871	0.8979	0.8852	**0.9371**
AA	93.5716	94.2521	94.2510	94.5944	94.8010	94.5761	95.1731	94.4737	**96.4714**

accuracy. These findings not only affirm the effectiveness of our approach but also underscore its potential in automating HSI quality assessment and band reconstruction, all without the need for manual prefiltering of noisy bands.

ACKNOWLEDGEMENT

This work was supported in part by the Guangdong Province Key Construction Discipline Scientific Research Ability Promotion Project (2022ZDJS015) and the National Natural Science Foundation Major Project of China (42192580).

CONFLICT OF INTEREST STATEMENT

The authors certify that there is no conflicts of interest.

DATA AVAILABILITY STATEMENT

Our study utilised two publicly available datasets. All data used in this research are openly accessible and can be found at the following sources https://www.ehu.eus/ccwintco/index.php?title=Hyperspectral_Remote_Sensing_Scenes.

ORCID

Ping Ma https://orcid.org/0000-0003-3687-364X

REFERENCES

1. Li, Y., et al.: ABBD: accumulated band-wise binary distancing for unsupervised parameter-free hyperspectral change detection. IEEE J. Sel. Top. Appl. Earth Obs. Rem. Sens. 17, 9880–9893 (2024). https://doi.org/10.1109/jstars.2024.3407212
2. Yan, Y., et al.: Nondestructive quantitative measurement for precision quality control in additive manufacturing using hyperspectral imagery and machine learning. IEEE Trans. Ind. Inf. 20(8), 9963–9975 (2024). https://doi.org/10.1109/tii.2024.3384609
3. Zheng, X., et al.: Rotation-invariant attention network for hyperspectral image classification. IEEE Trans. Image Process. 31, 4251–4265 (2022). https://doi.org/10.1109/tip.2022.3177322
4. Ma, P., et al.: Automatic geolocation and measuring of offshore energy infrastructure with multimodal satellite data. IEEE J. Ocean. Eng. 49(1), 66–79 (2023). https://doi.org/10.1109/joe.2023.3319741
5. Li, Y., et al.: SSA-LHCD: a singular spectrum analysis-driven lightweight network with 2-D self-attention for hyperspectral change detection. Rem. Sens. 16(13), 2353 (2024). https://doi.org/10.3390/rs16132353
6. Ma, P., et al.: Multiscale superpixelwise prophet model for noise-robust feature extraction in hyperspectral images. IEEE Trans. Geosci. Rem. Sens. 61, 1–12 (2023). https://doi.org/10.1109/tgrs.2023.3260634
7. Yan, Y., et al.: PCA-domain fused singular spectral analysis for fast and noise-robust spectral-spatial feature mining in hyperspectral classification. Geosci. Rem. Sens. Lett. IEEE 20, 1–5 (2021). https://doi.org/10.1109/lgrs.2021.3121565
8. Sheikh, H.R., Sabir, M.F., Bovik, A.C.: A statistical evaluation of recent full reference image quality assessment algorithms. IEEE Trans. Image Process. 15(11), 3440–3451 (2006). https://doi.org/10.1109/tip.2006.881959
9. Mittal, A., Soundararajan, R., Bovik, A.C.: Making a "completely Blind" image quality analyzer. IEEE Signal Process. Lett. 20(3), 209–212 (2013). https://doi.org/10.1109/lsp.2012.2227726
10. Venkatanath, N., et al.: Blind image quality evaluation using perception based features. In: 2015 Twenty First National Conference on Communications (NCC), pp. 1–6 (2015)
11. Wang, Z., et al.: Image quality assessment: from error visibility to structural similarity. IEEE Trans. Image Process. 13(4), 600–612 (2004). https://doi.org/10.1109/tip.2003.819861

12. Huang, Y., et al.: Enhancing image watermarking with adaptive embedding parameter and PSNR guarantee. IEEE Trans. Multimed. 21(10), 2447–2460 (2019). https://doi.org/10.1109/tmm.2019.2907475
13. Luo, X., et al.: Unsupervised band selection method based on importance-assisted column subset selection. IEEE Access 7, 517–527 (2018). https://doi.org/10.1109/access.2018.2885545
14. Cao, X., et al.: Hyperspectral band selection with objective image quality assessment. Int. J. Rem. Sens. 38(12), 3656–3668 (2017). https://doi.org/10.1080/01431161.2017.1302110
15. Sun, K., et al.: A new band selection method for hyperspectral image based on data quality. IEEE J. Sel. Top. Appl. Earth Obs. Rem. Sens. 7(6), 2697–2703 (2014). https://doi.org/10.1109/jstars.2014.2320299
16. Tian, J., Philpot, W.D.: Relationship between surface soil water content, evaporation rate, and water absorption band depths in SWIR reflectance spectra. Remote Sens. Environ. 169, 280–289 (2015). https://doi.org/10.1016/j.rse.2015.08.007
17. Das, B., et al.: Evaluation of different water absorption bands, indices and multivariate models for water-deficit stress monitoring in rice using visible-near infrared spectroscopy. Spectrochim. Acta Part A Mol. Biomol. Spectrosc. 247, 119104 (2021). https://doi.org/10.1016/j.saa.2020.119104
18. Sun, L., et al.: Fast superpixel based subspace low rank learning method for hyperspectral denoising. IEEE Access 6, 12031–12043 (2018). https://doi.org/10.1109/access.2018.2808474
19. Fan, F., et al.: Hyperspectral image denoising with superpixel segmentation and low-rank representation. Inf. Sci. 397, 48–68 (2017). https://doi.org/10.1016/j.ins.2017.02.044
20. Sidorov, O., Yngve Hardeberg, J.: Deep hyperspectral prior: single-image denoising, inpainting, super-resolution. In: Proceedings of the IEEE/CVF International Conference on Computer Vision Workshops (2019)
21. Shi, Q., et al.: Hyperspectral image denoising using a 3-D attention denoising network. IEEE Trans. Geosci. Rem. Sens. 59(12), 10348–10363 (2021). https://doi.org/10.1109/tgrs.2020.3045273
22. Cao, X., et al.: Deep spatial-spectral global reasoning network for hyperspectral image denoising. IEEE Trans. Geosci. Rem. Sens. 60, 1–14 (2022). https://doi.org/10.1109/tgrs.2021.3069241
23. Zhou, Y., et al.: For-backward LSTM-based missing data reconstruction for time-series Landsat images. GIScience Remote Sens. 59(1), 410–430 (2022). https://doi.org/10.1080/15481603.2022.2031549
24. Czerkawski, M., et al.: Deep internal learning for inpainting of cloud-affected regions in satellite imagery. Rem. Sens. 14(6), 1342 (2022). https://doi.org/10.3390/rs14061342
25. Zhang, Y., et al.: A coarse-to-fine framework for cloud removal in remote sensing image sequence. IEEE Trans. Geosci. Rem. Sens. 57(8), 5963–5974 (2019). https://doi.org/10.1109/tgrs.2019.2903594
26. Zhang, Q., et al.: Missing data reconstruction in remote sensing image with a unified spatial–temporal–spectral deep convolutional neural network. IEEE Trans. Geosci. Rem. Sens. 56(8), 4274–4288 (2018). https://doi.org/10.1109/tgrs.2018.2810208
27. Zhang, Q., et al.: Thick cloud and cloud shadow removal in multitemporal imagery using progressively spatio-temporal patch group deep learning. ISPRS J. Photogrammetry Remote Sens. 162, 148–160 (2020). https://doi.org/10.1016/j.isprsjprs.2020.02.008
28. Perry, M.B.: The weighted moving average technique. Wiley Encycl. Oper. Res. Manage. Sci. (2010)
29. Laouafi, A., Laouafi, F., Boukelia, T.E.: An adaptive hybrid ensemble with pattern similarity analysis and error correction for short-term load forecasting. Appl. Energy 322, 119525 (2022). https://doi.org/10.1016/j.apenergy.2022.119525
30. Wang, Z., Zhao, Y., He, L.: Forecasting the monthly iron ore import of China using a model combining empirical mode decomposition, nonlinear autoregressive neural network, and autoregressive integrated moving average. Appl. Soft Comput. 94, 106475 (2020). https://doi.org/10.1016/j.asoc.2020.106475
31. Zabalza, J., et al.: Singular spectrum analysis for effective feature extraction in hyperspectral imaging. Geosci. Rem. Sens. Lett. IEEE 11, 1886–1890 (2014)
32. Zabalza, J., et al.: Novel two-dimensional singular spectrum analysis for effective feature extraction and data classification in hyperspectral imaging. IEEE Trans. Geosci. Rem. Sens. 53(8), 4418–4433 (2015). https://doi.org/10.1109/tgrs.2015.2398468
33. Mei, S., et al.: Hyperspectral image classification using attention-based bidirectional long short-term memory network. IEEE Trans. Geosci. Rem. Sens. 60, 1–12 (2021). https://doi.org/10.1109/tgrs.2021.3102034
34. Li, Q., et al.: Ensemble EMD-based spectral-spatial feature extraction for hyperspectral image classification. IEEE J. Sel. Top. Appl. Earth Obs. Rem. Sens. 13, 5134–5148 (2020). https://doi.org/10.1109/jstars.2020.3018710
35. Ma, P., et al.: Multiscale 2-D singular spectrum analysis and principal component analysis for spatial–spectral noise-robust feature extraction and classification of hyperspectral images. IEEE J. Sel. Top. Appl. Earth Obs. Rem. Sens. 14, 1233–1245 (2021). https://doi.org/10.1109/jstars.2020.3040699
36. Taylor, S.J., Letham, B.: Forecasting at scale. Am. Statistician 72(1), 37–45 (2018). https://doi.org/10.1080/00031305.2017.1380080
37. Mittal, A., Moorthy, A.K., Bovik, A.C.: No-reference image quality assessment in the spatial domain. IEEE Trans. Image Process. 21(12), 4695–4708 (2012). https://doi.org/10.1109/tip.2012.2214050
38. Sharifi, K., Leon-Garcia, A.: Estimation of shape parameter for generalized Gaussian distributions in subband decompositions of video. IEEE Trans. Circ. Syst. Video Technol. 5(1), 52–56 (1995). https://doi.org/10.1109/76.350779
39. Lasmar, N., Stitou, Y., Berthoumieu, Y.: Multiscale skewed heavy tailed model for texture analysis. In: 2009 16th IEEE International Conference on Image Processing, pp. 2281–2284. ICIP) (2009)
40. Schölkopf, B., et al.: New support vector algorithms. Neural Comput. 12(5), 1207–1245 (2000). https://doi.org/10.1162/089976600300015565
41. Chang, C., Lin, C.: LIBSVM: a library for support vector machines. ACM Trans. Intell. Syst. Technol. 2(3), 1–27 (2011). https://doi.org/10.1145/1961189.1961199
42. Chow, L.S., Rajagopal, H.: Modified-BRISQUE as no reference image quality assessment for structural MR images. Magn. Reson. Imaging 43, 74–87 (2017). https://doi.org/10.1016/j.mri.2017.07.016
43. Fang, L., et al.: Classification of hyperspectral images by exploiting spectral–spatial information of superpixel via multiple kernels. IEEE Trans. Geosci. Rem. Sens. 53(12), 6663–6674 (2015). https://doi.org/10.1109/tgrs.2015.2445767
44. Achanta, R., et al.: SLIC superpixels compared to state-of-the-art superpixel methods. IEEE Trans. Pattern Anal. Mach. Intell. 34(11), 2274–2282 (2012). https://doi.org/10.1109/tpami.2012.120
45. Yu, H., et al.: Multiscale superpixel-level subspace-based support vector machines for hyperspectral image classification. Geosci. Rem. Sens. Lett. IEEE 14(11), 2142–2146 (2017). https://doi.org/10.1109/lgrs.2017.2755061
46. Green, R.O., et al.: Imaging spectroscopy and the airborne visible/infrared imaging spectrometer (AVIRIS). Remote Sens. Environ. 65(3), 227–248 (1998). https://doi.org/10.1016/s0034-4257(98)00064-9
47. Wald, L.: Data fusion: definitions and architectures: fusion of images of different spatial resolutions. Presses des MINES (2002)
48. Zabalza, J., et al.: Fast implementation of two-dimensional singular spectrum analysis for effective data classification in hyperspectral imaging. J. Franklin Inst. 355(4), 1733–1751 (2018). https://doi.org/10.1016/j.jfranklin.2017.05.020
49. Cover, T., Hart, P.: Nearest neighbor pattern classification. IEEE Trans. Inf. Theor. 13(1), 21–27 (1967). https://doi.org/10.1109/tit.1967.1053964

How to cite this article: Ma, P., et al.: Hyperspectral imagery quality assessment and band reconstruction using the prophet model. CAAI Trans. Intell. Technol. 1–15 (2024). https://doi.org/10.1049/cit2.12373